GEOPHYSICS, VOL. 75, NO. 2 (MARCH-APRIL 2010); P. R21–R35, 12 FIGS., 3 TABLES.
10.1190/1.3294570

Improved resolution in Bayesian lithology/fluid inversion from prestack seismic data and well observations: Part 1 — Methodology

Marit Ulvmoen[1] and Henning Omre[1]

ABSTRACT

The focus of our study is lithology/fluid inversion with spatial coupling from prestack seismic amplitude variation with offset (AVO) data and well observations. The inversion is defined in a Bayesian setting where the complete solution is the posterior model. The prior model for the lithology/fluid (LF) characteristics is defined as a profile Markov random-field model with lateral continuity. Each vertical profile is further given as an inhomogeneous Markov-chain model upward through the reservoir. The likelihood model is defined by profile, and it relates the LF characteristics to the seismic data via a set of elastic material parameters and a convolution model. The likelihood model is approximated. The resulting approximate posterior model is explored using an efficient block Gibbs simulation algorithm. The inversion approach is evaluated on a synthetic realistic 2D reservoir. Seismic AVO data and well observations are integrated in a consistent manner to obtain predictions of the LF characteristics with associated uncertainty statements. The predictions appear very reliable despite the approximation of the posterior model, and errors in seismic data are the major contributions to the uncertainty. Resolution of the inversion is improved considerably by using a spatially coupled prior LF model, and LF units of 1–3 ms thick can be identified even with a seismic signal-to-noise ratio of two. The inversion results appear robust toward varying model parameter values in the prior model as a result of the discretization of LF characteristics and seismic data with good spatial coverage.

INTRODUCTION

Predicting lithology/fluid (LF) characteristics in a petroleum reservoir with associated uncertainty is important when developing reserves. Normally, LF characteristics are predicted based on geologic understanding of the reservoir combined with well observations and seismic data. The classification problem is ill posed because several LF configurations may produce the same seismic data. The objective of our study is to infer LF classes in a target zone, given well observations and seismic amplitude variation with offset (AVO) data. The inversion is defined in a Bayesian setting where prior knowledge about the LF characteristics is combined with information contained in the observed data.

Bayesian frameworks are commonly used to invert LF characteristics from prestack seismic data. In Eidsvik et al. (2004), the inversion is defined in a horizontal 2D setting where the prior is a Markov random field. In this horizontal 2D model, vertical couplings resulting from convoluting the seismic data are ignored. A multivariate approach to fluid-unit inversion is presented in Contreras et al. (2005). The inversion methodology is applied to a real data set in a thorough empirical study. Their spatial model appears to be Gaussian and continuous. In Larsen et al. (2006), the inversion is defined in a 1D vertical setting where the vertical dependencies within the LF classes are modeled as a Markov-chain prior model. The inversion is solved approximately, including vertical deconvolution of the seismic data. In Buland et al. (2008), the inversion is solved in a 3D setting using a vertically coupled likelihood model and a locationwise (or based upon location) prior model, which entails that no prior spatial information about the LF classes is taken into account. In González et al. (2008), an algorithmic approach to lithology inversion from stacked seismic data is defined. The approach is based on a multipoint spatial prior model for lithology and sequential trial-and-error conditioning to the seismic data. The conditioning procedure may be very computer demanding and is expected to be unfeasible for high-dimensional AVO seismic data needed to classify fluid filling. Moreover, the efficiency of the conditioning is unclear because of lack of formality in defining the algorithm. In Bosch et al. (2009), stacked seismic data and well observations are combined in a spatial model, but only porosity and saturation are modeled as continuous variables in a Gaussian setting. For a thorough introduction to LF inversion from seismic data, see Avseth et al. (2005).

Manuscript received by the Editor 9 February 2009; revised manuscript received 14 August 2009; published online 9 April 2010.
[1]Norwegian University of Science and Technology, Trondheim, Norway. E-mail: ulvmoen@math.ntnu.no; omre@math.ntnu.no.

In our current study, the inversion is solved using a categorical, spatially coupled prior model for the LF classes. This model formulation appears to be more in accordance with geologists' understanding of the reservoir geometry; moreover, LF observations in wells have influence beyond the well locations. One particular focus is identifying thin, laterally extensive features of the reservoir, defined in our study as shale units. A categorical, spatially coupled prior model for the LF classes will improve resolution in the inversion.

The target zone is discretized into vertical profiles and lateral horizons. Vertical couplings of the LF classes are modeled by a Markov-chain prior model. Lateral continuity of the LF classes in the horizons is further modeled by a profile Markov random-field model. We assume the 3D LF model falls within the class of Markov random fields (see Winkler, 1995). A Markov random field is defined by a set of local continuity measures, and it enforces some spatial smoothness on the posterior model. The local nature of the model provides flexibility to reproduce spatially varying proportions and continuity directions and to adapt to data with good spatial coverage. Moreover, the continuity couples the spatial data and, hence, reduces the effect of noise in the data. These features are favorable for inverting seismic data and well observations into LF classes.

The likelihood model is approximated such that the upward-downward algorithm used to assess the posterior model in Larsen et al. (2006) can be used to explore the vertical profiles. Laterally, a block Gibbs simulation algorithm is used. Realizations and prediction of the most probable combination of LF classes with associated uncertainties can be assessed by simulation-based inference. Our study draws heavily on previous work on seismic AVO inversion (Buland and Omre, 2003a; Larsen et al., 2006).

The major contribution of our study is to expand the model in Larsen et al. (2006) into three dimensions, where lateral continuity of the LF classes is modeled. We demonstrate that by modeling lateral continuity, considerably better resolution in LF class prediction can be obtained. The inversion approach is evaluated empirically on synthetic seismic data. The approach is further evaluated on real seismic data from a reservoir offshore Norway in Ulvmoen et al. (this issue).

NOTATION

We denote the target zone in three dimensions by $\mathcal{D}$ and let it be discretized by the lattice $\mathcal{L}_\mathcal{D}$ divided into vertical profiles and lateral horizons. The profiles are discretized downward by the regular lattice $\mathcal{L}_\mathcal{D}^t$:$\{1,\ldots,T\}$, where the two-way reflection time t corresponds to the seismic sampling. The lateral horizons are further discretized by the regular lattice $\mathcal{L}_\mathcal{D}^\mathbf{x}$, with $\mathcal{L}_\mathcal{D}^\mathbf{x}$ corresponding to the seismic-survey positions.

The LF characteristic in lattice node $(\mathbf{x},t) \in \mathcal{L}_\mathcal{D}$ is denoted as $\pi_{\mathbf{x},t}$, discretized into a set of LF classes $\pi_{\mathbf{x},t} \in \{\pi^1,\ldots,\pi^L\}$. The complete set of LF classes in the 3D target zone is further represented by $\boldsymbol{\pi}$:$\{\pi_{\mathbf{x},t};(\mathbf{x},t) \in \mathcal{L}_\mathcal{D}\}$.

We assume well observations to be available along vertical well profiles at n well locations represented by $\mathcal{K} \subset \mathcal{L}_\mathcal{D}^\mathbf{x}$, which coincide with some of the lattice locations in $\mathcal{L}_\mathcal{D}^\mathbf{x}$. The well data are denoted by $\mathbf{d}^w$; they contain information about the LF classes at $t \in \mathcal{L}_\mathcal{D}^t$ along the well profiles. The well observations originally were observed on a finer depth resolution, and conversion into the current time resolution must be made. The uncertainty in this conversion should be captured by the well likelihood model.

The seismic data are assumed to be true-amplitude processed such that the prestack amplitudes represent band-limited primary reflection strengths. The data are also assumed to be prestack migrated and transformed from offsets to reflection angles. The seismic prestack gather is represented by $\mathbf{d}^s$ containing the seismic samples in $\mathcal{L}_\mathcal{D}$ for a set of reflection angles $\boldsymbol{\theta}$:$\{\theta_1^\circ,\ldots,\theta_n^\circ\}$. The uncertainty of this preprocessing should be captured by the seismic likelihood model. The joint well observations and seismic data are denoted by $\mathbf{d}$:$\{\mathbf{d}^w,\mathbf{d}^s\}$.

An isotropic, elastic medium is completely described by three elastic parameters: P-wave velocity, S-wave velocity, and density. To link the LF classes and the seismic data, elastic properties are defined at each location in $\mathcal{L}_\mathcal{D}$. Let $\boldsymbol{m}_{\mathbf{x},t}$ represent the log transform of the three elastic parameters in lattice node $(\mathbf{x},t) \in \mathcal{L}_\mathcal{D}$. The complete set of elastic parameters is represented by $\mathbf{m}$:$\{\mathbf{m}_{\mathbf{x},t};(\mathbf{x},t) \in \mathcal{L}_\mathcal{D}\}$.

The term $p(\cdot)$ is used as a generic term for probability. In particular, $p(\pi_{\mathbf{x},t})$ denotes the probability for the various LF classes $\pi_{\mathbf{x},t} \in \{\pi^1,\ldots,\pi^L\}$. Correspondingly, $p(\boldsymbol{\pi})$ is a multivariate probability for $\boldsymbol{\pi}$, the complete set of LF classes. For discrete variables, $p(\cdot)$ will be the probability mass function (PMF), although it will be the probability density function (PDF) for continuous variables. Moreover, the probability for $\boldsymbol{\pi}$ given $\mathbf{d}$ is denoted by $p(\boldsymbol{\pi}|\mathbf{d})$.

STOCHASTIC MODEL

The objective of our study is to predict the LF characteristics in a target zone from well observations and seismic prestack data. We do this in a Bayesian setting, combining available prior knowledge about $\boldsymbol{\pi}$ with the information contained in the data $\mathbf{d}$. In this setting, the complete solution is the posterior model, which is expressed as

$$p(\boldsymbol{\pi}|\mathbf{d}) = \text{const} \times p(\mathbf{d}|\boldsymbol{\pi})p(\boldsymbol{\pi}), \tag{1}$$

where $p(\mathbf{d}|\boldsymbol{\pi})$ is the likelihood model and $p(\boldsymbol{\pi})$ is the prior model. The constant is a normalizing constant that is usually difficult to determine; hence, the posterior model is normally explored through stochastic simulation where direct calculation of the constant is avoided. From the posterior model, the probability of any combination of LF classes in the target zone can be calculated; in particular, the most probable combination can be identified. It is also possible to generate a set of realizations of the LF characteristics representing the prediction uncertainty. These realizations can be considered as possible LF configurations.

Likelihood model

The likelihood model defines the likelihood of the LF classes given well observations and seismic data. We assume the well observations and seismic data are to be collected independently; this entails conditional independence between well and seismic data, expressed

by

$$p(\mathbf{d}|\boldsymbol{\pi}) = p(\mathbf{d}^w|\boldsymbol{\pi})p(\mathbf{d}^s|\boldsymbol{\pi}), \tag{2}$$

where $p(\mathbf{d}^w|\boldsymbol{\pi})$ is a well likelihood model and $p(\mathbf{d}^s|\boldsymbol{\pi})$ is a seismic likelihood model.

The well likelihood model is defined from locationwise observations of LF characteristics along the well profiles, given by

$$[d^w_{\mathbf{x},t}|\pi_{\mathbf{x},t}] = \mu_{\pi_{\mathbf{x},t}} + e^w_{\mathbf{x},t}, \tag{3}$$

where $\mu_{\pi_{\mathbf{x},t}}$ is the expected well observation response for LF class $\pi_{\mathbf{x},t}$ and $e^w_{\mathbf{x},t}$ is a spatially independent Gaussian error term. The relation defines the likelihood model

$$p(\mathbf{d}^w|\boldsymbol{\pi}) = \prod_{\mathbf{x}\in\mathcal{K}}\prod_t p(d^w_{\mathbf{x},t}|\pi_{\mathbf{x},t}), \tag{4}$$

where $\mathcal{K}$ are the well locations in $\mathcal{L}^{\mathbf{x}}_{\mathcal{D}}$ and the product in t is taken over $\mathcal{L}^t_{\mathcal{D}}$.

A decomposition such as in Larsen et al. (2006) is used in the seismic likelihood model. It is expressed as

$$p(\mathbf{d}^s|\boldsymbol{\pi}) = \int \cdots \int p(\mathbf{d}^s|\mathbf{m})p(\mathbf{m}|\boldsymbol{\pi})d\mathbf{m}, \tag{5}$$

where $p(\mathbf{d}^s|\mathbf{m})$ is a seismic likelihood model and $p(\mathbf{m}|\boldsymbol{\pi})$ is a rock-physics likelihood model. The integral is over the three elastic parameters in the target zone; hence, it is computationally demanding to determine.

The rock-physics likelihood model can be factorized as

$$p(\mathbf{m}|\boldsymbol{\pi}) = \prod_{\mathbf{x}}\prod_t p(\mathbf{m}_{\mathbf{x},t}|\pi_{\mathbf{x},t}), \tag{6}$$

with $\mathbf{x}$ taken over $\mathcal{L}^{\mathbf{x}}_{\mathcal{D}}$ and t taken over $\mathcal{L}^t_{\mathcal{D}}$ when not explicitly expressed. Hence, the rock-physics model is assumed to depend only on colocated LF variables (see Avseth et al., 2005).

The relation between $\mathbf{d}^s$ and $\mathbf{m}$ is defined by the vertical convolution model as in Buland and Omre (2003a):

$$[\mathbf{d}^s|\mathbf{m}] = \mathbf{WADm} + \mathbf{e}, \tag{7}$$

where $\mathbf{A}$ is a matrix of angle-dependent, weak-contrast Aki-Richards coefficients (see Aki and Richards, 1980), $\mathbf{D}$ is a differential matrix giving the contrasts of the elastic properties in $\mathbf{m}$, $\mathbf{W}$ is a block-diagonal convolution matrix containing one wavelet for each time-angle gather, and $\mathbf{e}$ is Gaussian observation error. Using this relation, the seismic likelihood model is expressed as in Larsen et al. (2006):

$$p(\mathbf{d}^s|\mathbf{m}) = \text{const} \times \frac{p_*(\mathbf{m}|\mathbf{d}^s)}{p_*(\mathbf{m})}, \tag{8}$$

where const is a general constant and $p_*(\mathbf{m}|\mathbf{d}^s)$ and $p_*(\mathbf{m})$ are Gaussian posterior and prior PDFs for linearized Zoeppritz AVO inversion (see Buland and Omre, 2003a). The posterior PDF $p_*(\mathbf{m}|\mathbf{d}^s)$ can be calculated extremely fast in the Fourier domain (see Buland et al., 2003). The justification for the decomposition is discussed in Larsen et al. (2006).

Prior model

The prior model contains a priori knowledge about the 3D LF characteristics in the reservoir before any observations are made. Horizontally, we expect the LF characteristics to have extensive continuity, isotropic or anisotropic. The LF characteristics are further expected to appear in certain sequences vertically because lithologies are generated by sedimentary processes and fluids are segregated by gravity. Hence, the ordering of LF classes should be modeled nonsymmetrically and nonstationary in the vertical direction. To model this a priori information about the LF classes, we define the prior model to be a profile Markov random field.

The profile Markov random field is defined by

$$p(\boldsymbol{\pi}_{\mathbf{x}}|\boldsymbol{\pi}_{-\mathbf{x}}) = p(\boldsymbol{\pi}_{\mathbf{x}}|\boldsymbol{\pi}_{\mathbf{y}};\mathbf{y}\in\delta(\mathbf{x})); \text{ all } \mathbf{x}\in\mathcal{L}^{\mathbf{x}}_{\mathcal{D}}, \tag{9}$$

where $\boldsymbol{\pi}_{\mathbf{x}}:\{\pi_{\mathbf{x},t};t\in\mathcal{L}^t_{\mathcal{D}}\}$ is a vertical LF profile in an arbitrary $\mathbf{x}$ in $\mathcal{L}^{\mathbf{x}}_{\mathcal{D}}$, $\boldsymbol{\pi}_{-\mathbf{x}}:\{\boldsymbol{\pi}_{\mathbf{y}};\mathbf{y}\in\mathcal{L}^{\mathbf{x}}_{\mathcal{D}},\mathbf{y}\neq\mathbf{x}\}$ is the set of all LF profiles except $\boldsymbol{\pi}_{\mathbf{x}}$, and $\delta(\mathbf{x})$ is a fixed neighborhood around $\mathbf{x}$ in $\mathcal{L}^{\mathbf{x}}_{\mathcal{D}}$. Hence, given all LF classes in the target zone except in profile $\boldsymbol{\pi}_{\mathbf{x}}$, the LF profile $\boldsymbol{\pi}_{\mathbf{x}}$ is dependent only upon the LF profiles in a predefined neighborhood $\delta(\mathbf{x})$ around $\mathbf{x}$. According to the Hammersley-Clifford theorem, the set of all conditional models fully specifies the Markov random field $p(\boldsymbol{\pi})$ (see Winkler, 1995).

To model vertical orderings of the fluids, we let the LF profiles $\boldsymbol{\pi}_{\mathbf{x}}$ be defined by nonhomogeneous Markov-chain models upward through the target zone:

$$p(\boldsymbol{\pi}_{\mathbf{x}}|\boldsymbol{\pi}_{\mathbf{y}};\mathbf{y}\in\delta(\mathbf{x})) = \prod_t p(\pi_{\mathbf{x},t}|\pi_{\mathbf{x},t+1},\pi_{\mathbf{y},t};\mathbf{y}\in\delta(\mathbf{x}));$$
$$\text{all } \mathbf{x}\in\mathcal{L}^{\mathbf{x}}_{\mathcal{D}}, \tag{10}$$

with $p(\pi_{\mathbf{x},T}|\pi_{\mathbf{x},T+1},\pi_{\mathbf{y},T};\mathbf{y}\in\delta(\mathbf{x})) = p(\pi_{\mathbf{x},T}|\pi_{\mathbf{y},T};\mathbf{y}\in\delta(\mathbf{x}))$ for notational convenience. This Markov-chain model corresponds to the model in Larsen et al. (2006), where it is demonstrated to be reliable in modeling petroleum reservoirs.

The upward transition probabilities for LF classes between two horizons in a profile, i.e., from $t+1$ to t, can be expressed as the transition matrix $\mathbf{P}^t(\pi_{\mathbf{y},t};\mathbf{y}\in\delta(\mathbf{x}))$, where the elements are the conditional $p(\pi_{\mathbf{x},t}|\pi_{\mathbf{x},t+1},\pi_{\mathbf{y},t};\mathbf{y}\in\delta(\mathbf{x}))$ for all configurations of $(\pi_{\mathbf{x},t},\pi_{\mathbf{x},t+1})$. The transition matrices are dependent on the time reference t through $\{\pi_{\mathbf{y},t};\mathbf{y}\in\delta(\mathbf{x})\}$; hence, the Markov chain is nonhomogeneous.

In Appendix A, we demonstrate that the assumptions made for the profile Markov random field entail that

$$p(\pi_{\mathbf{x},t}|\boldsymbol{\pi}_{-(\mathbf{x},t)}) = p(\pi_{\mathbf{x},t}|\pi_{\mathbf{x},t-1},\pi_{\mathbf{x},t+1},\pi_{\mathbf{y},t};\mathbf{y}\in\delta(\mathbf{x}));$$
$$\text{all } (\mathbf{x},t)\in\mathcal{L}_{\mathcal{D}}, \tag{11}$$

with $\boldsymbol{\pi}_{-(\mathbf{x},t)}:\{\pi_{\mathbf{y},s};(\mathbf{y},s)\in\mathcal{L}_{\mathcal{D}},(\mathbf{y},s)\neq(\mathbf{x},t)\}$. Hence, $\boldsymbol{\pi}$ is a Markov random field in the traditional sense (see Winkler, 1995). This property can be used to ensure that the prior model is consistent in a probabilistic sense.

There are, however, several advantages in defining the prior model as a profile Markov random field. Dependency structures in the lateral and vertical directions are clearly separated, which is suitable for reservoir modeling. Dependencies in the vertical direction can be formulated as a nonsymmetric, nonstationary Markov chain suitable for modeling sedimentary processes and gravity segregation of fluids. Furthermore, a simulation algorithm that allows analytical treatment in the vertical direction and requires only an iterative proce-

dure in the horizontal domain can be defined. However, the local nature of Markov random fields makes them very flexible, which complicates simulation when conditioning information is not available.

The prior profile Markov random-field model is defined with references in an orthogonal system of axes. Continuities in petroleum reservoirs do not necessarily coincide with these axis directions. Lithology continuity mostly follows structural surfaces; fluid continuity mostly follows lateral gravity surfaces. Moreover, expected proportions of lithologies and fluids often have vertical trends. The local nature of the profile Markov random-field definition adapts to different continuity directions and expected proportion trends. The neighborhood $\delta(\mathbf{x})$ can be extended, and the neighborhood influence of the transition probabilities can be different for lithologies and fluids to account for different continuity directions. Local adaption of the transition probabilities can also capture varying expected proportions of LF classes. Some of these features of the prior model are demonstrated in the real case study in Part II of this paper (Ulvmoen et al., this issue).

The assessment of the transition probabilities in the prior model is of course a challenge. The vertical transitions can be inferred from well observations, but lateral dependencies must be determined from outcrop studies or training images. Estimation of model parameters in Markov random fields is frequently discussed in statistical literature (see Winkler, 1995). If training images are available, we recommend using a pseudolikelihood approach to assess model parameters. Finally, varying expected proportions must be inferred from regional geologic understanding.

Posterior model

The posterior model is uniquely defined by the likelihood and prior models. It is given by

$$p(\boldsymbol{\pi}|\mathbf{d}) = \text{const} \times \prod_{\mathbf{x}\in\mathcal{K}}\prod_{t} p(d^{w}_{\mathbf{x},t}|\pi_{\mathbf{x},t}) \times \left[\int \cdots \int \frac{p_*(\mathbf{m}|\mathbf{d}^s)}{p_*(\mathbf{m})}\prod_{\mathbf{x}}\prod_{t} p(\mathbf{m}_{\mathbf{x},t}|\pi_{\mathbf{x},t})d\mathbf{m}\right] p(\boldsymbol{\pi}), \tag{12}$$

where const is a normalizing constant. The normalizing constant defined by $\Sigma_{\boldsymbol{\pi}} p(\boldsymbol{\pi}|\mathbf{d}) = 1$ is computationally demanding to determine because it is the sum over all combinations of LF classes in the target zone. The integral is over all configurations of the three elastic parameters in the target zone; hence, it is very difficult to determine. An approximation along the lines of Larsen et al. (2006) makes the expression partly analytically tractable and reduces the dimension of the integral.

In the approximation, the Gaussian PDFs $p_*(\mathbf{m})$ and $p_*(\mathbf{m}|\mathbf{d}^s)$ are calculated based upon profile (profilewise). Further, correlations within $\mathbf{m}_{\mathbf{x}}$ and $[\mathbf{m}_{\mathbf{x}}|\mathbf{d}^s_{\mathbf{x}}]$ are ignored, and only the diagonal elements of the covariance matrices in the Gaussian PDFs $p_*(\mathbf{m}_{\mathbf{x}})$ and $p_*(\mathbf{m}_{\mathbf{x}}|\mathbf{d}^s_{\mathbf{x}})$ are used. This approximation is proven reliable in the 1D case in Ulvmoen and Hammer (2010), where it is demonstrated that the approximation captures between 50% and 90% of the information content in the likelihood for typical seismic inversion problems.

The approximate posterior model is expressed

$$\tilde{p}(\boldsymbol{\pi}|\mathbf{d}) = \text{const} \times \prod_{\mathbf{x}\in\mathcal{K}}\prod_{t} p(d^{w}_{\mathbf{x},t}|\pi_{\mathbf{x},t})\prod_{\mathbf{x}}\prod_{t} l(\mathbf{d}^s_{\mathbf{x}}|\pi_{\mathbf{x},t})p(\boldsymbol{\pi}), \tag{13}$$

where

$$l(\mathbf{d}^s_{\mathbf{x}}|\pi_{\mathbf{x},t}) = \int\int\int \frac{p_*(\mathbf{m}_{\mathbf{x},t}|\mathbf{d}^s_{\mathbf{x}})}{p_*(\mathbf{m}_{\mathbf{x},t})} p(\mathbf{m}_{\mathbf{x},t}|\pi_{\mathbf{x},t})d\mathbf{m}_{\mathbf{x},t} \tag{14}$$

is the approximated likelihood model. The recursive algorithm in Larsen et al. (2006) can now be applied; the integral is of dimension three and numerically tractable.

The prior model follows a Markov random-field model. Hence, with a likelihood function that factorizes, we know (Winkler, 1995) that the associated approximate conditional posterior model can be expressed as

$$\tilde{p}(\boldsymbol{\pi}_{\mathbf{x}}|\boldsymbol{\pi}_{-\mathbf{x}},\mathbf{d}_{\mathbf{x}}) = \begin{cases} \text{const} \times \prod_t l(\mathbf{d}^s_{\mathbf{x}}|\pi_{\mathbf{x},t})p(\pi_{\mathbf{x},t}|\pi_{\mathbf{x},t+1},\pi_{\mathbf{y},t};\mathbf{y}\in\delta(\mathbf{x})); \\ \qquad\qquad \text{all } \mathbf{x}\in -\mathcal{K} \\ \text{const} \times \prod_t p(d^w_{\mathbf{x},t}|\pi_{\mathbf{x},t})l(\mathbf{d}^s_{\mathbf{x}}|\pi_{\mathbf{x},t})p(\pi_{\mathbf{x},t}|\pi_{\mathbf{x},t+1},\pi_{\mathbf{y},t};\mathbf{y}\in\delta(\mathbf{x})); \\ \qquad\qquad \text{all } \mathbf{x}\in\mathcal{K} \end{cases} \tag{15}$$

with the set $-\mathcal{K}$ containing all elements in $\mathcal{L}^{\mathbf{x}}_{\mathcal{D}}$ except the ones in $\mathcal{K}$, i.e., all horizon locations except the well locations. We use this block Markov formulation of the posterior model to define an efficient simulation algorithm.

ASSESSMENT OF POSTERIOR MODEL

In expression 15, conditional posterior models are defined for all $\mathbf{x}\in\mathcal{L}^{\mathbf{x}}_{\mathcal{D}}$. These conditional posterior models are on the same form as the 1D posterior model in Larsen et al. (2006) except for the inhomogeneneity in the prior model. The upward-downward recursive algorithm used to explore the posterior model in Larsen et al. (2006), however, is also valid for nonhomogeneous Markov-chain prior models (see Chib, 1996). Hence, the conditional model in expression 15 can be simulated exactly by the efficient upward-downward recursive algorithm. Laterally, a block Gibbs simulation algorithm may be used because the profile Markov random field is specified by a complete set of multivariate conditional models. In the Gibbs simulation algorithm, direct computation of the normalizing constant is avoided.

The Gibbs simulation algorithm is described fully in Appendix B, and an outline of the algorithm follows.

Simulation algorithm

```
Initiate
  Generate arbitrary π
Iterate
  Draw x uniform randomly from L_D^x
  Generate π_x from p̃(π_x|π_{-x},d_x) by the
  upward-downward simulation algorithm
```

The algorithm converges such that, in the limit, $\boldsymbol{\pi}$ will be a realization from $\tilde{p}(\boldsymbol{\pi}|\mathbf{d})$. Although the model is defined in three dimen-

sions, the iterative Gibbs simulation algorithm only operates in two dimensions. The third dimension is simulated exactly by the very fast recursive upward-downward algorithm. To have all grid nodes updated once, also termed one sweep, the number of operations is proportional to the square of the number of LF classes times the number of grid nodes in $\mathcal{L}_{\mathcal{D}}$. The convergence rate of the algorithm is highly model specific and it will be discussed in the following section.

SYNTHETIC EMPIRICAL STUDY

In the empirical study on a realistic synthetic test case, we focus on two aspects. First, we evaluate the general quality of the inversion approach. The LF characteristics are simulated and predicted from seismic AVO data with low signal-to-noise ratio (S/N) and from a seismic AVO signal without observation error. Second, we evaluate the ability to identify thin, laterally extensive layers of shale. This identification is made possible by improved resolution in the inversion. These thin layers of shale are particularly important because they greatly impact fluid flow.

We perform an empirical study on a reference 2D synthetic reservoir that we have made manually. The reference reservoir $\boldsymbol{\pi}$ contains the four LF classes: gas-saturated sandstone, oil-saturated sandstone, brine-saturated sandstone, and shale (Figure 1). The target zone is defined from 2000 to 2284 ms vertically, discretized into units of 1 ms, corresponding to the seismic sampling density; hence, $T = 284$. Horizontally, 100 common-midpoint (CMP) profiles are considered. The synthetic reference reservoir is thicker than usual reservoirs, and it contains several sequences of shale and sandstone with separate fluid regimes. This vertical repeatability is enforced to randomize over error terms and to minimize border effects on top and bottom caused by the convolution. The proportions of the four LF classes — gas-, oil-, and brine-saturated sandstone and shale — are (0.18, 0.23, 0.37, 0.22). In the reservoir, many layers of shale are thin with variable lateral extensions. These shale layers, ranging 1–3 ms thick, are much thinner than in Larsen et al. (2006) and far below what is normally referred to as seismic resolution of approximately 10 ms.

The prior model is defined as a profile Markov random field, with the profiles defined as inhomogeneous Markov-chain models upward through the reservoir as described earlier. We term this model a 2D Markov random field. The transitions up the profiles in $\mathbf{x} \in \mathcal{L}_{\mathcal{D}}^{\mathbf{x}}$, given the rest of the field, are expressed as the transition matrices $\mathbf{P}^t(\pi_{\mathbf{y},t};\mathbf{y} \in \delta(\mathbf{x}))$, where the elements are the conditional $p(\pi_{\mathbf{x},t} | \pi_{\mathbf{x},t+1}, \pi_{\mathbf{y},t};\mathbf{y} \in \delta(\mathbf{x}))$ for all (4×4) configurations of $(\pi_{\mathbf{x},t}, \pi_{\mathbf{x},t+1})$.

We consider a first-order neighborhood in each lateral direction such that $\delta(\mathbf{x}) = (\mathbf{x} - 1, \mathbf{x} + 1)$, giving 16 possible neighborhood configurations. By lateral symmetry, the number of configurations is reduced to 10. The transition matrices are constructed such that most probability is assigned to transitions into LF classes identical to the neighboring ones and low probability to other transitions. The transition matrix neighbored by oil-saturated sandstone and shale is, for example,

$$\mathbf{P}^t_{\mathrm{SO,SH}} = \begin{pmatrix} 0.0005 & 0 & 0 & 0.9995 \\ 0.0002 & 0.4999 & 0 & 0.4999 \\ 0.0002 & 0.4998 & 0.0002 & 0.4998 \\ 0.0002 & 0.4998 & 0.0002 & 0.4998 \end{pmatrix},$$

with rows and columns corresponding to gas-, oil-, and brine-saturated sandstone and shale, respectively. The transitions with zero probability in the matrix are the same as in Larsen et al. (2006), and they ensure ordering of the fluids according to gravity. These transition matrices are specified independent of the reference reservoir, and the intent is to capture prior knowledge about lateral continuity of LF variables and vertical fluid ordering. We use the limiting distribution of the transition matrices as initial distributions. All transition matrices and corresponding limiting distributions are fully described in Appendix C.

If we average these ten transition matrices and compute the corresponding limiting distribution, we obtain (0.35, 0.18, 0.12, 0.35). This distribution can be seen as an approximation of the prior proportions of gas-, oil-, and brine-saturated sandstone and shale, implicitly defined by the prior model. These proportions deviate considerably from the proportions in the reference reservoir: (0.18, 0.23, 0.37, 0.22). We use schematic prior transition matrices that capture lateral LF continuities and vertical fluid orderings. If training images are available, these transition matrices can be assessed by a pseudo-likelihood approach (see Winkler, 1995).

In Larsen et al. (2006), the inversion model is defined profilewise, and the approximate posterior model is calculated exactly by the recursive upward-downward algorithm. In our study, a more time-consuming Gibbs sampling must be used. We also apply the profilewise Markov-chain prior model defined in Larsen et al. (2006) and compare the results to the 2D prior Markov random-field model of the current study. For the profilewise Markov-chain prior model, the stationary transition matrix is calculated from the reference reservoir. The transition matrix and corresponding limiting distribution are specified in Appendix C. We also use a locationwise prior model without spatial coupling (see Larsen et al., 2006). In this prior model, the limiting distribution in the profilewise Markov-chain model is used. This limiting distribution corresponds to the fraction of each LF class in the reference reservoir.

We use well observations in two well locations $\mathcal{K}$:{20,80}. The well observations $\mathbf{d}^w$ are exact observations of LF classes along the profiles presented in Figure 2. The proportions of the four LF classes in the well observations are (0.15, 0.19, 0.30, 0.36), which are fairly different from the reservoir proportions. The shale content is more than 1.5 times larger in the wells than in the entire reservoir. This de-

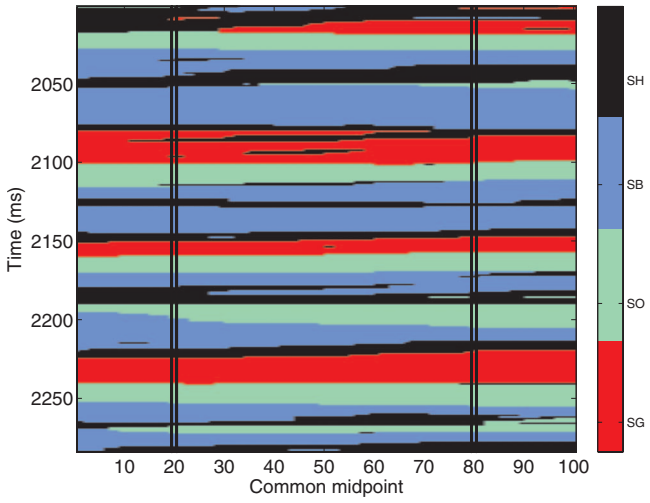

Figure 1. Reference LF characteristics $\boldsymbol{\pi}$.

viation is caused by sampling uncertainty because the wells only cover 2% of the lattice nodes. The well likelihood model is defined from exact locationwise observations of these LF characteristics.

The rock-physics likelihood model $p(\mathbf{m}_{\mathbf{x},t}|\pi_{\mathbf{x},t})$ is a function in the three elastic parameters — P-wave velocity, S-wave velocity, and density — for each LF class. As in Larsen et al. (2006), a set of representative samples from a probabilistic rock-physics model is defined to link the LF classes and the elastic parameters. The samples are presented in Figure 3. The elastic properties corresponding to the reference reservoir are obtained by using the mean value of $[\mathbf{m}_{\mathbf{x},t}|\pi_{\mathbf{x},t}]$ from the samples at each location and adding appropriate heterogeneity to make $\mathbf{m}$ appear realistic. The mean values for P-wave velocity, S-wave velocity, and density are (3141, 1794, 2182), (3199, 1758, 2274), (3365, 1749, 2312), and (3521, 1894, 2555) (in m/s, m/s, kg/m^3) for gas-, oil-, and brine-saturated sandstone and shale, respectively.

The seismic likelihood model $p(\mathbf{d}^s|\mathbf{m})$ is defined by a profilewise Aki-Richards convolutional model as in Buland and Omre (2003a). The seismic signal is generated profilewise for the five incidence angles $\boldsymbol{\theta} = (0°, 10°, 20°, 30°, 40°)$ and a Ricker wavelet with frequency of 30 Hz and length of 61 ms discretized over $\mathcal{L}'_{\mathcal{D}}$ for all time-angle gathers. Note that the model accounts for angle-dependent wavelets if that is required. The observation error contains a mixture of zero-mean vertical-wavelet colored noise and white noise (see Buland and Omre, 2003a), and the variance in the colored noise is 100 times the variance in the white noise. The observation error is generated profilewise, then added to the seismic signal resulting in the seismic data. The S/N in the seismic data is calculated as the ratio between the variance in the seismic signal and the variance in the observation error, and the value is 2.0.

Figure 4 displays the synthetic prestack seismic data $\mathbf{d}^s$. This data set is based on the empirical rock-physics model, a convolutional linearized Zoeppritz model, and a wavelet colored error term. The error term captures randomized uncertainty in the data, but systematic errors in the forward seismic model are not accounted for. For thin LF units and large angles above 30°, the systematic errors may have some impact (see Mallick, 2007), but this is ignored here. Real seismic data must be preprocessed to obtain AVO seismic data, and the uncertainty associated with this is assumed to be captured in the error term. Exact assessment of the parameters in these error terms is of course difficult; but if reliable well observations are available, these parameters can be estimated (see Buland and Omre, 2003b). This provides more reliable uncertainty assessments in real studies.

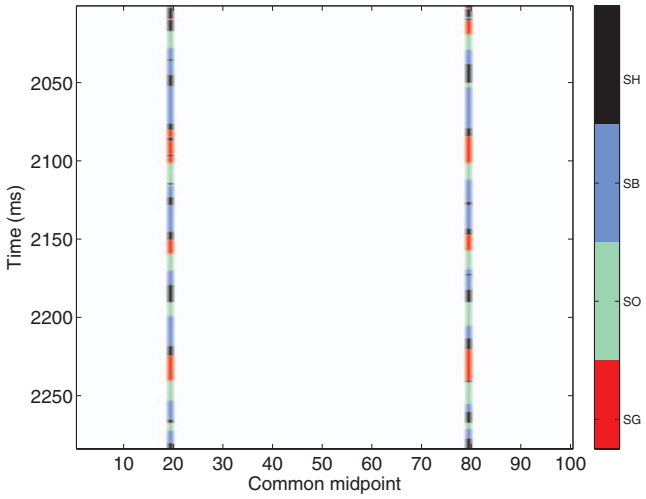

Figure 2. Well observations $\mathbf{d}^w$ in $\mathcal{K}$:{20,80}.

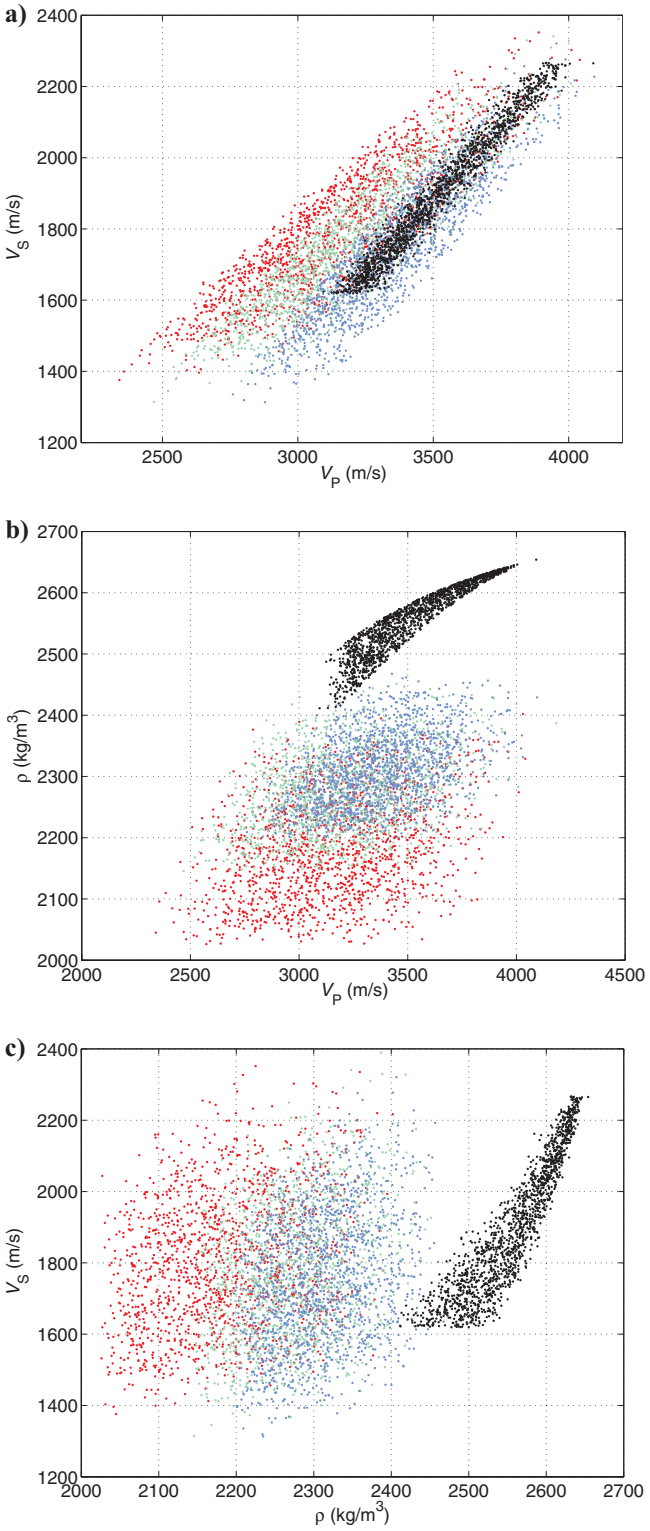

Figure 3. Elastic properties exp($\mathbf{m}$) represented by P-wave velocity V_P, S-wave velocity V_S, and density ρ given gas-saturated sandstone (red), oil-saturated sandstone (green), brine-saturated sandstone (blue), and shale (black) simulated from a rock-physics model.

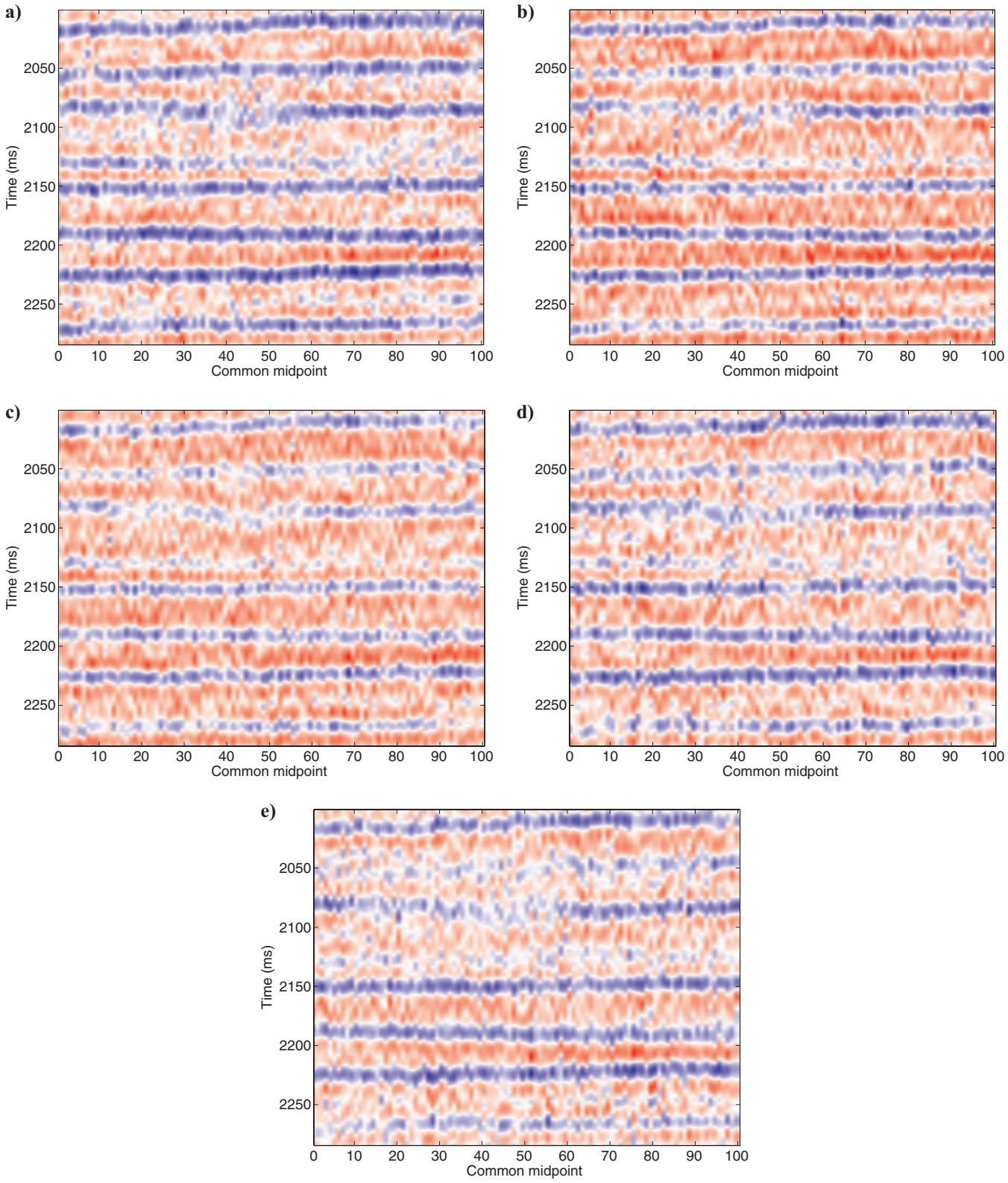

Figure 4. Synthetic prestack seismic data $\mathbf{d}^s$ for angles $\boldsymbol{\theta} = (0°, 10°, 20°, 30°, 40°)$ in (a), (b), (c), (d), and (e), respectively.

Real seismic AVO data appear with more laterally correlated errors, probably from the preprocessing, but we have chosen to generate data with the likelihood model used in the inversion and hence ignore lateral dependence in the error term. The logarithm of the elastic material properties in $\mathbf{m}$ are approximated by a Gaussian random field parameterized by $(\mu_*,\Sigma_*,c_*(\tau))$ as expectation vector, covariance matrix, and spatial correlation function, respectively. The former two are calculated from the reference elastic parameters using standard statistical estimators, with values

$$\boldsymbol{\mu}_* = (8.117,7.500,7.770)$$

and

$$\boldsymbol{\Sigma}_* = \begin{pmatrix} 0.0075 & 0.0080 & 0.0035 \\ 0.0080 & 0.0114 & 0.0030 \\ 0.0035 & 0.0030 & 0.0043 \end{pmatrix},$$

corresponding to the logarithm of P-wave velocity, S-wave velocity, and density, respectively. We use a second-order exponential spatial correlation function $c_*(\tau)$ with range of 3 ms. The integral in the likelihood model is obtained as the average of the functional value in 3000 samples specified for $[\mathbf{m}_{\mathbf{x},t}|\pi_{\mathbf{x},t}]$.

In the implementation of the algorithm, 30 ms of shale are added to the top and the bottom of the reservoir to avoid boundary effects. As lateral boundary conditions, we assume that the left- and rightmost profiles have the same neighbor profiles on both sides, and the neighbor profiles are hence given double weights on the borders. We initiate the algorithm from four extreme configurations of $\boldsymbol{\pi}$ containing one class only and monitor the proportion of the LF classes after each sweep with one sweep corresponding to one update of each profile in the field.

The sample paths are shown in Figure 5. All of the initial configurations converge to very similar proportions after 2000 sweeps, which is defined to be the burn-in period. The mixing of the algorithm, which characterizes the ability to cover the sample space of the posterior model, can still be poor, however. The stable pattern of the sample path for the range of 2000–20,000 sweeps and the good spatial coverage of seismic data, together with analytical deconvolution in the simulation algorithm, make us believe that mixing is not a major problem in the algorithm. The sample paths indicate that the posterior model has one unique mode, which is not surprising, given the large amount of seismic data with good spatial coverage. Convergence will be even faster if a profilewise inversion is used as the initial state. The simulation algorithm is very fast, and it is well suited for parallel implementation. Therefore, computer demands do not appear as a major problem for 2D inversion. In 3D problems, however, mixing may be slower.

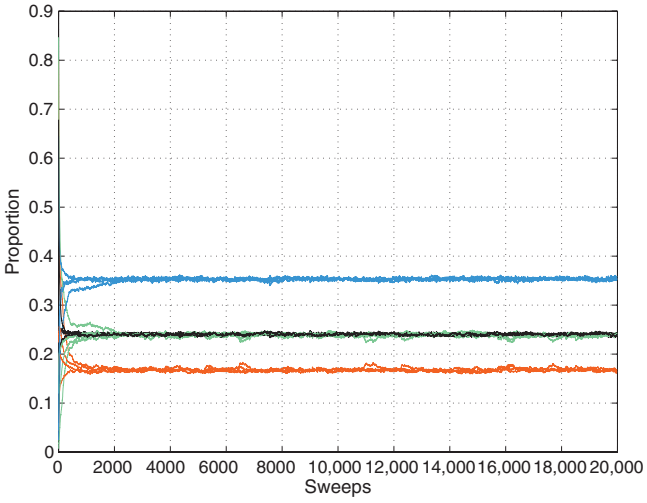

Figure 5. Convergence plot monitoring the proportion of LF classes after each sweep of simulation algorithm.

RESULTS WITH DISCUSSION

The empirical study is based on a synthetic, manually designed 2D reference reservoir. The well observations are obtained by copying the LF classes in the reference reservoir along the well traces. The seismic AVO data are obtained by using the seismic likelihood model, which is later used in the inversion algorithm. The prior LF model is obtained independent of the reference reservoir and is designed to capture major LF characteristics. The impact of using different prior models is demonstrated in this study.

The uncertainty assessment only represents uncertainties in the predicted LF characteristics given the observations under the known exact model. Loss in predictability because of the approximation of the posterior model is also captured. More realistic uncertainty assessment in studies of real reservoirs can be made by estimating the model parameters from the reservoir observations (see Buland and Omre, 2003b). Conclusions from our study will help geoscientists determine the proper model formulation.

Our study focuses on the LF characteristics $\boldsymbol{\pi}$. The complete solution is defined to be the approximate posterior model $\tilde{p}(\boldsymbol{\pi}|\mathbf{d})$, from which realizations can be generated and the most probable combination of LF characteristics can be determined. The marginals $\tilde{p}(\pi_{\mathbf{x},t}|\mathbf{d})$ are estimated by counting the number of occurrences of each LF class at each location over 3600 realizations taken every 20 sweeps after burn-in. We calculate the locationwise most probable solution from the expression

$$\hat{\pi}_{\mathbf{x},t} = \arg\max_{\pi_{\mathbf{x},t}}\{\tilde{p}(\pi_{\mathbf{x},t}|\mathbf{d})\};\ \text{all}\ (\mathbf{x},t) \in \mathcal{L}_{\mathcal{D}}. \qquad (16)$$

Figure 6 contains three independent realizations of LF characteristics generated from the approximate posterior model $\tilde{p}(\boldsymbol{\pi}|\mathbf{d})$. Each realization can be considered as possible LF characteristics, and the set of realizations represents the posterior uncertainty in the solution. The structure in the realizations is the same, and all of the realizations are realistic with respect to fluid segregation. The deviation between the realizations is small, indicating little posterior uncertainty.

Figure 7 compares the predicted LF characteristics $\hat{\boldsymbol{\pi}}$ as the locationwise most probable solution and the reference LF characteristics $\boldsymbol{\pi}$. Table 1 presents the associated classification matrix. In a perfect prediction, $\hat{\boldsymbol{\pi}}$ would be identical to $\boldsymbol{\pi}$ and the classification matrix would contain zeroes in all entries except on the diagonal. The structure in the predicted solution and the reference case is mostly the same, but the reference LF characteristics are slightly more homogeneous than the locationwise most probable solution. On the other hand, the most probable solution is more homogeneous than the realizations caused by uncertainty in the model. The well observations do not stand out, indicating that the inversion model is reliable in near-well areas and that the information contained in the wells is an

integral part of the inversion solution. The fluid segregation condition is fulfilled.

All of the diagonal elements in the classification matrix are the largest, and the proportions of the LF classes are largely correct. The proportions in the LF prediction are (0.17, 0.24, 0.36, 0.23), compared to the proportions in the reference reservoir of (0.18, 0.23, 0.37, 0.22). Recall that the approximate prior proportions in the prior model are (0.35, 0.18, 0.12, 0.35) and that the proportions in the well observations are (0.15, 0.19, 0.30, 0.36). We interpret this adjustment of proportions from the prior model to be caused by conditioning on the seismic AVO data, and the inversion is fairly robust toward the choice of prior model. One main challenge of the study is to

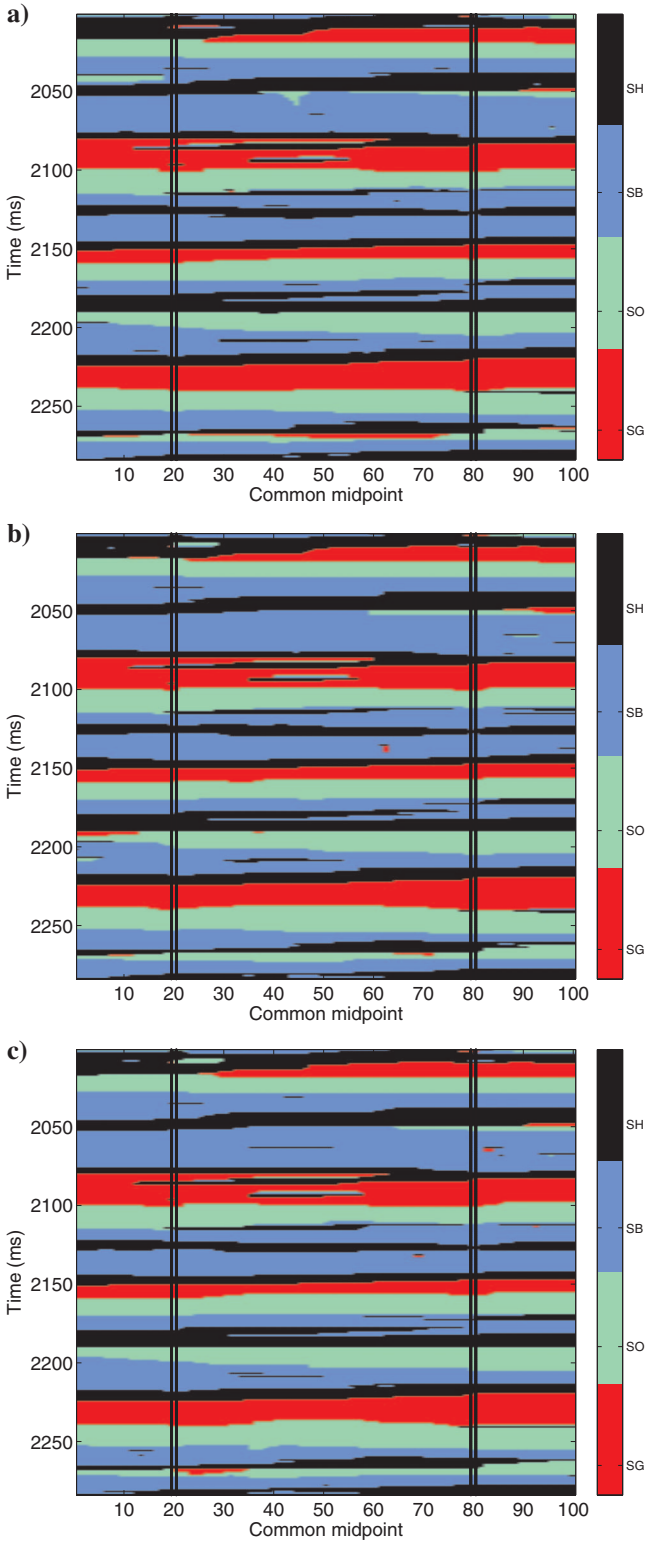

Figure 6. Independent realizations of LF characteristics from approximate posterior $\tilde{p}(\boldsymbol{\pi}|\mathbf{d})$ for 2D Markov random-field model.

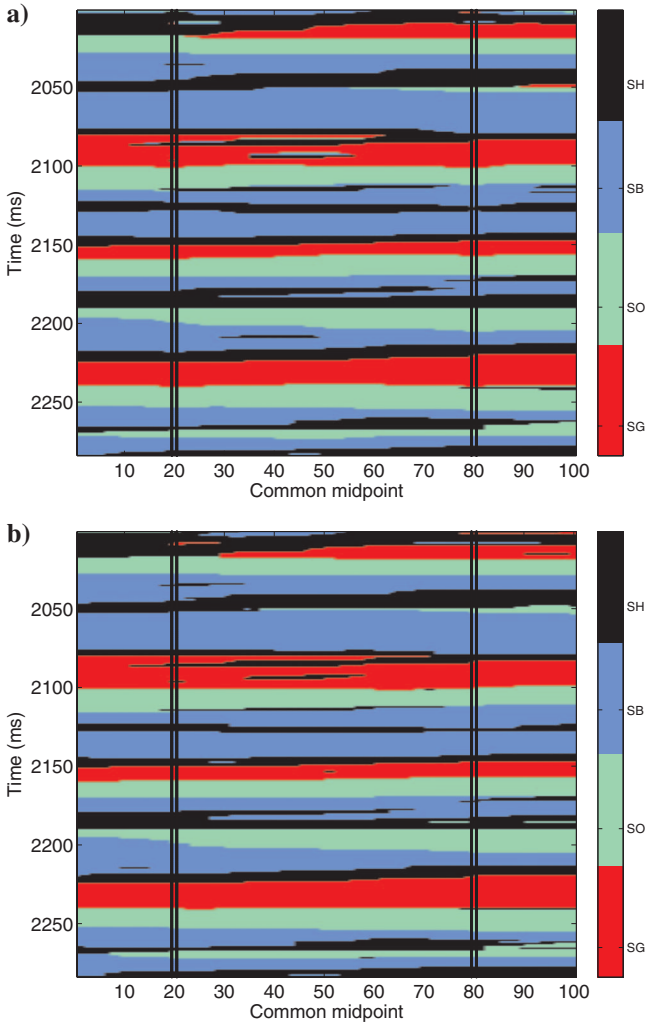

Figure 7. (a) Locationwise most probable LF characteristics prediction $\hat{\boldsymbol{\pi}}$ for 2D Markov random-field model; (b) reference LF characteristics $\boldsymbol{\pi}$.

Table 1. Classification matrix for 2D Markov random-field model.

$\boldsymbol{\pi}\backslash\hat{\boldsymbol{\pi}}$	SG	SO	SB	SH	Σ
SG	4605	365	42	13	5025
SO	94	6265	126	36	6521
SB	0	83	9798	639	10,520
SH	51	44	169	6070	6334
Σ	4750	6757	10,135	6758	

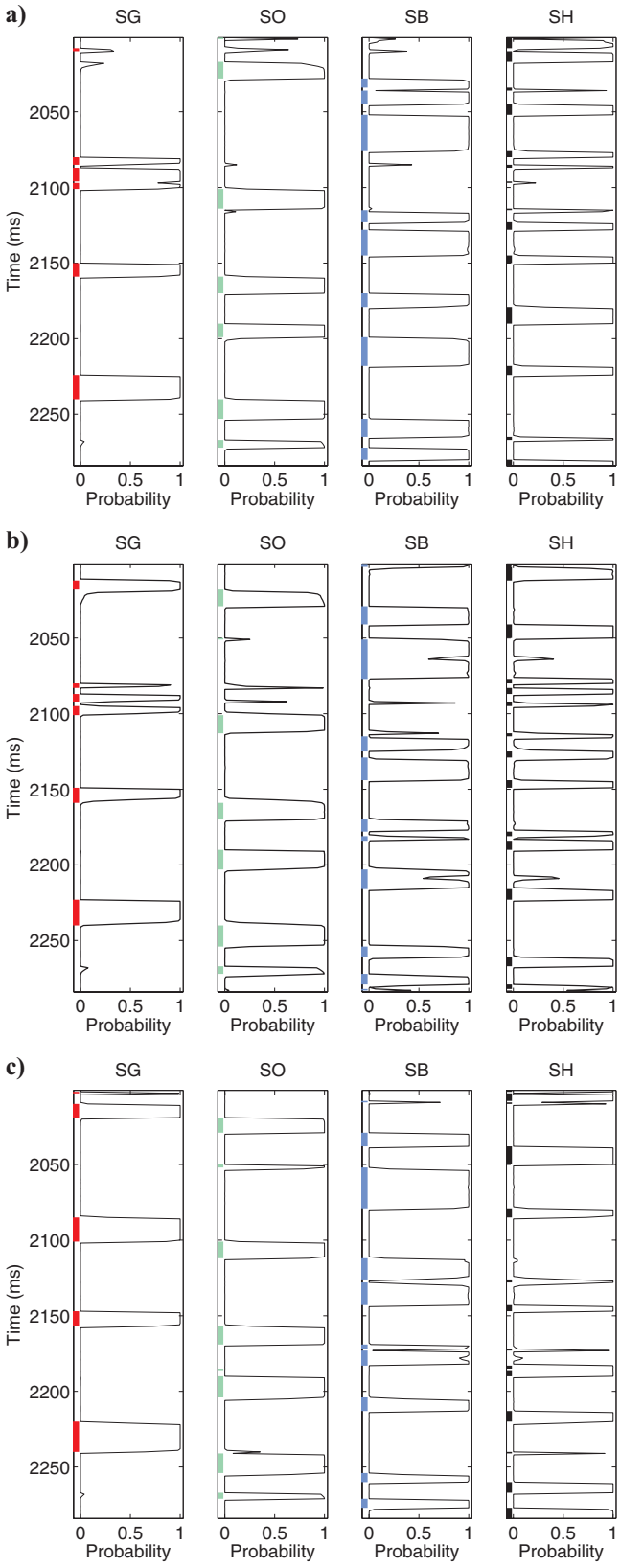

Figure 8. Marginal approximate posterior $\tilde{p}(\pi_{\mathbf{x},t}|\mathbf{d})$ for 2D Markov random-field model in profiles $\mathbf{x}$:{21,50,79} in (a), (b), and (c), respectively. The reference LF profile $\boldsymbol{\pi}_{\mathbf{x}}$ is marked on each axis.

classify thin layers of shale, and we see from the prediction that layers down to 1 ms are identified. This is caused by the spatial coupling in the prior model, which increases the probability of identification from modeling lateral continuity of shales. A few shale units are missed and a few artificial shale units are added, but the heterogeneity is primarily correct.

Figure 8 compares profiles $\mathbf{x}$:{21,50,79} of the marginal approximate posterior model $\tilde{p}(\pi_{\mathbf{x},t}|\mathbf{d})$ with the reference LF classes marked on the respective axes. The former and latter profiles are to the right and left of the two wells, respectively; profile $\mathbf{x}$:{50} is in the middle of the target zone. In a perfect classification, the probabilities would be one in the positions of the reference LF classes and zero otherwise. It is difficult to distinguish the near- and off-well profiles by visual inspection. Both profile types imply high probability of classification to the true classes even for thin layers, and the probability of correct classification increases with increasing layer thickness. All shale layers are found with high probability — even the ones that are very thin. The few misclassifications occur with reduced probability.

Figure 9 and Table 2 compare the predicted LF characteristics from three different prior models; the 2D Markov random-field prior model, the profilewise Markov-chain prior model, and the locationwise prior model. In the profilewise Markov-chain prediction, the vertical orderings are correct with respect to fluid segregation. The well observations are not integrated in the solution, and we observe a skyline effect from lack of horizontal continuity. The diagonal elements in the classification matrix are not always the largest, and the proportions of the LF classes deviate from the reference. The shale layers are often too thick, and thin sandstone layers between two layers of shale are filled with shale in many locations. The shale layers are thinner, and the prediction is much more homogeneous in the 2D Markov random field than in the profilewise Markov-chain model.

Much of the improvement in the 2D Markov random-field model relative to the profilewise Markov-chain model is in classifying gas-saturated sandstone, where spatial coupling in the prior model increases the probability of identification. This is verified in the classification matrices. The locationwise prediction is very heterogeneous. However, it is possible to recognize the structure from the reference reservoir, particularly the shale layers. Even though the locationwise prior model is independent in each location, the likelihood model is calculated given the full dimension of the seismic data including deconvolution.

The prediction is better than one could expect from a traditional spatially independent model. The proportion of brine-saturated sandstone is overestimated, but gas-saturated sandstone is severely underestimated. There is little horizontal continuity, and the fluid segregation condition is not fulfilled. The elements on the diagonal of the classification matrix are often small compared to the off-diagonal ones, and the proportions of the classes are incorrect. Thin layers of shale are often indicated in the prediction, but many artificial shale locations are added. The 2D Markov random-field prediction is much more homogeneous than the locationwise prediction. Much of the gain in the 2D Markov random-field model is in classification of gas- and oil-saturated sandstone and in classification of thin shale layers.

Figure 10 compares the marginal approximate posterior model $\tilde{p}(\pi_{\mathbf{x},t}|\mathbf{d})$ in profile $\mathbf{x}$:{50} for the three prior models. The probabilities in the profilewise Markov-chain model are smoothed between the layers, making the transitions indistinct. Most of the uncertainty

appears in these interfaces. The probabilities in the 2D Markov random-field model are closer to zero or one, and the probabilities are sharpened in the interfaces between the layers. The shale layers are thinner as a result of these sharpenings. The locationwise model has considerable fluctuation in the probabilities. Some probability of the correct LF class is often visible, indicating that the seismic data do contain some information regarding the LF classes. Most of the fluctuations are removed in the 2D Markov random-field model compared to the locationwise model.

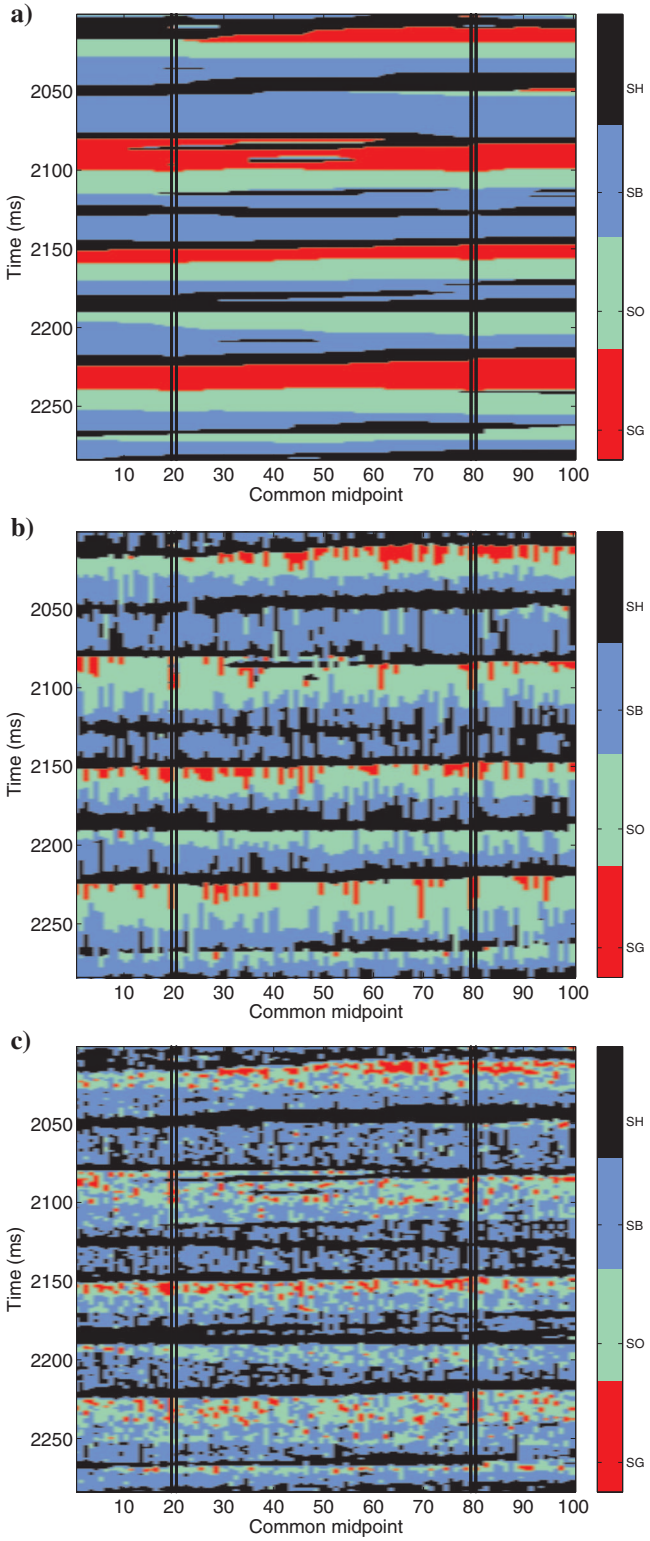

Figure 9. Locationwise most probable LF characteristics predictions $\hat{\boldsymbol{\pi}}$ for (a) 2D Markov random-field model, (b) profilewise Markov-chain model, and (c) locationwise model.

Figure 11 and Table 3 compare the predicted and reference LF characteristics from the inversion method based on the reference seismic signal without observation error. By visual inspection, the two are almost identical. The artificial layers of shale from the prediction with observation error are removed, and the shale layers have almost correct thickness. The numbers on the diagonal of the classification matrix are much larger than the off-diagonal ones, and the proportions of the LF classes are almost correct. The results indicate that the inversion method is very reliable and that the main problem is the noise in the observations.

Figure 12 compares the predicted LF characteristics based on different types of information. Recall that a prediction based on the prior profile Markov random-field model $p(\boldsymbol{\pi})$ conditioned on neither seismic nor well information is complicated because of the local nature of the prior model. The prediction based on well observations only, i.e., on the model $p(\boldsymbol{\pi}|\mathbf{d}^w)$, is displayed in Figure 12. The observations in the well trace are exactly reproduced, and they have large influence in the well-trace neighborhood. Farther away from the well trace, the prediction is mostly defined by the prior model and hence is very uncertain. The prediction based on seismic data only, i.e., on the model $p(\boldsymbol{\pi}|\mathbf{d}^s)$, is also displayed in Figure 12. By comparing this prediction to the reference LF characteristics, one ob-

Table 2. Classification matrix for 2D Markov random-field model, profilewise Markov-chain model, and locationwise model.

$\boldsymbol{\pi}\backslash\hat{\boldsymbol{\pi}}$	SG	SO	SB	SH	Σ
SG	4605	365	42	13	5025
SO	94	6265	126	36	6521
SB	0	83	9798	639	10,520
SH	51	44	169	6070	6334
Σ	4750	6757	10,135	6758	
$\boldsymbol{\pi}\backslash\hat{\boldsymbol{\pi}}$	SG	SO	SB	SH	Σ
SG	1069	3759	115	82	5025
SO	111	4382	1904	124	6521
SB	0	575	7500	2445	10520
SH	34	193	767	5340	6334
Σ	1214	8909	10,286	7991	
$\boldsymbol{\pi}\backslash\hat{\boldsymbol{\pi}}$	SG	SO	SB	SH	Σ
SG	921	2815	1258	31	5025
SO	217	2506	3594	204	6521
SB	3	300	6822	3395	10,520
SH	0	44	609	5681	6334
Σ	1141	5665	12,283	9311	

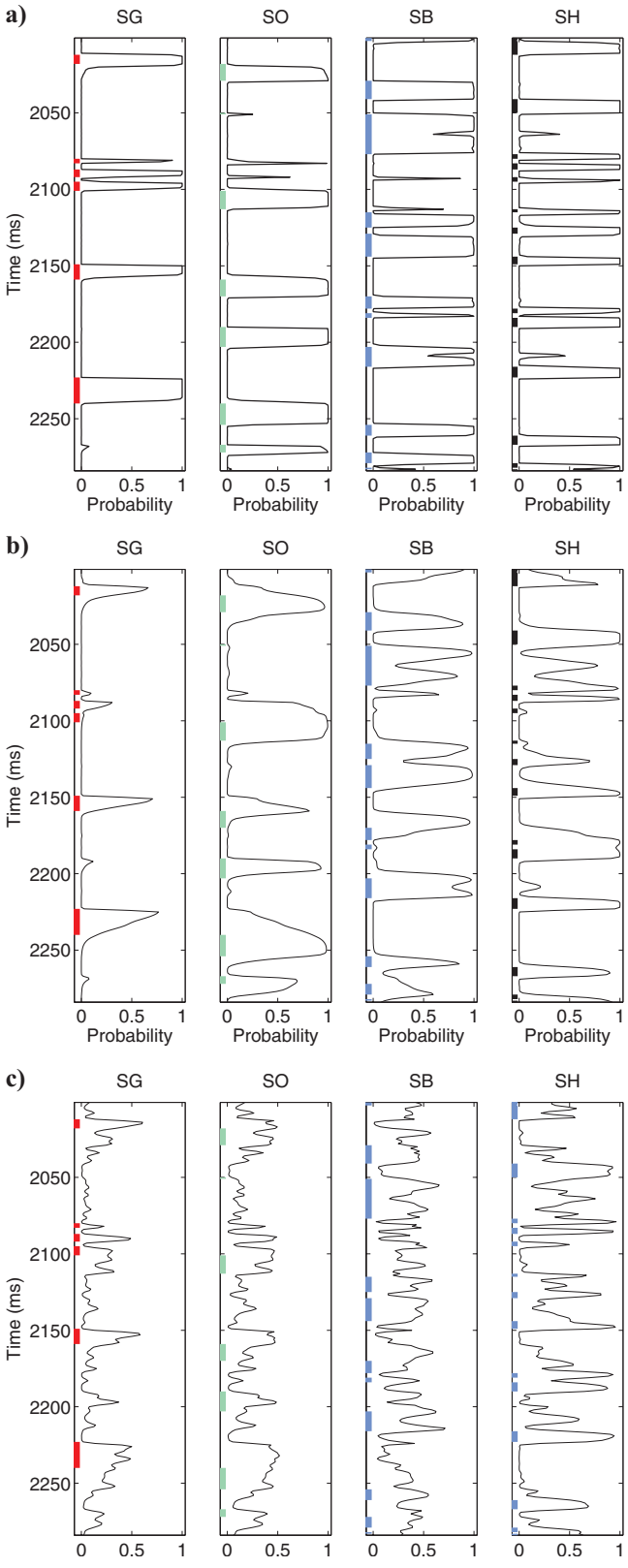

Figure 10. Marginal approximate posterior $\tilde{p}(\pi_{\mathbf{x},l}|\mathbf{d})$ in profile $\mathbf{x}$:{50} for (a) 2D Markov random-field model, (b) profilewise Markov-chain model, and (c) locationwise model. The reference LF profile $\boldsymbol{\pi}_{\mathbf{x}}$ is marked on each axis.

serves that the prediction is fairly reliable. Even thin shale units appear to be reproduced.

Thus, from the results, it is clear that the seismic data, not the well observations, provide the detailed structure in the solution. The well observations have impact only in the neighborhood of the well locations and by defining some fluid contacts.

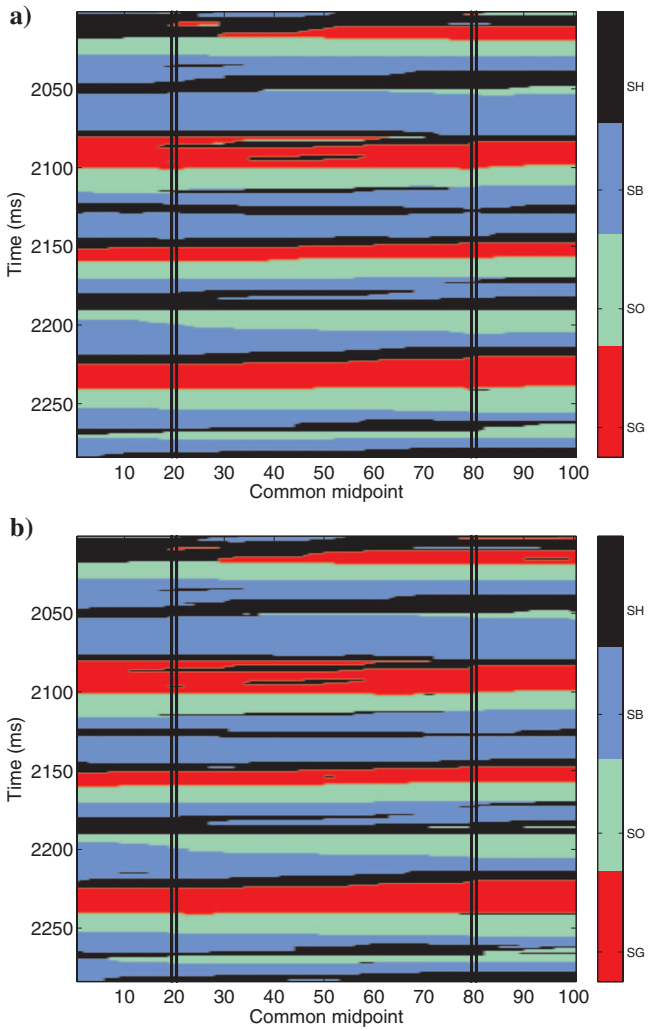

Figure 11. Results from case without observation error, i.e., inversion based on reference seismic signal $\mathbf{s}$. (a) Locationwise most probable LF characteristics prediction $\hat{\boldsymbol{\pi}}$ for 2D Markov random-field model; (b) reference LF characteristics $\boldsymbol{\pi}$.

Table 3. Classification matrix for inversion based on reference seismic signal s without observation error for 2D Markov random-field model.

$\boldsymbol{\pi}\backslash\hat{\boldsymbol{\pi}}$	SG	SO	SB	SH	Σ
SG	4702	318	0	5	5025
SO	0	6418	84	19	6521
SB	0	59	9950	511	10,520
SH	46	59	37	6192	6334
Σ	4748	6854	10,071	6727	

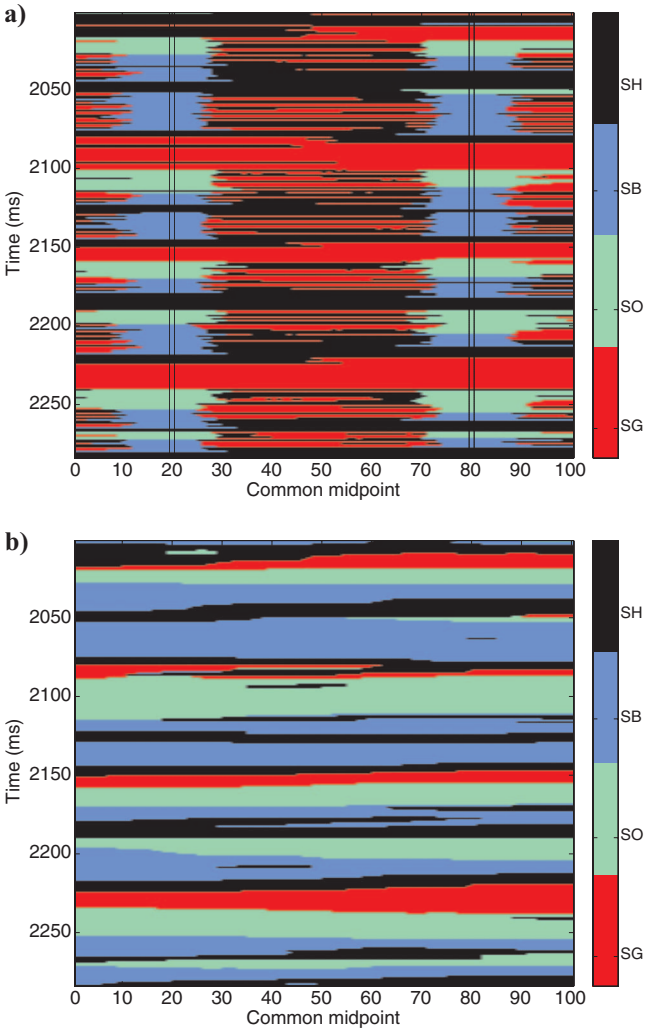

Figure 12. Locationwise most probable LF characteristics prediction $\hat{\boldsymbol{\pi}}$ for 2D Markov random-field model from (a) inversion based on well observations only and (b) inversion without well observations.

CONCLUSIONS

We have developed an efficient LF inversion approach from prestack seismic data and well observations for 3D reservoirs. The inversion is defined in a Bayesian framework where the prior model for the LF classes is defined as a profile Markov random field with the vertical profiles following Markov-chain models upward through the reservoir. The likelihood model is defined by a seismic forward model and rock-physics relations, and it is approximated to allow partial analytical treatment. The resulting posterior model is explored using an efficient block Gibbs simulation algorithm.

The inversion approach has been evaluated empirically on a 2D manually designed synthetic reservoir. The associated synthetic well observations and seismic AVO data are obtained by using the associated likelihood models, which are later used in the inversion. The prior LF models are obtained independent of the reference reservoir. Hence, the uncertainty assessments are made under a given exact model but also capturing uncertainty resulting from the approximation of the posterior model. In real studies, more representative uncertainty assessments can be obtained by estimating the model parameters from the available observations and training images.

The impact of using different prior LF models has been studied. We have compared the results from the fully coupled 2D Markov random-field model with results from profilewise and locationwise models. The 2D model combines seismic data and well observations, and the latter is given lateral influence beyond the well locations. The fully coupled 2D model provides more reliable results than the profilewise and locationwise models, and it provides reliable classifications even with an S/N of two. The proportions of the LF classes are precisely reproduced even with a prior model with biased prior proportions. LF units ranging 1–3 ms thick are identified by lateral continuity, and this is far below what is normally considered to be the seismic resolution in profilewise interpretation. The approximation in the likelihood model appears very reliable because the inversion is almost correct in the no-noise case. Hence, the observation error is the major source of uncertainty.

Frequently, LF inversion is referred to as an ill-posed inverse problem because of the lack of one unique solution. Our opinion, however, is that it is not severely ill posed. Seismic AVO data are abundant and LF classification is robust because of discretization. By introducing local neighboring rules through the prior profile Markov random field, we obtain very stable inversion results. Moreover, the results appear as robust with respect to deviations in the prior model as a result of abundance of seismic AVO data.

The 3D simulation algorithm is very efficient because it is based on an analytical solution vertically, and Markov-chain Monte-Carlo simulation is needed only in two dimensions laterally. Hence, the algorithm is feasible to perform in three dimensions.

The LF inversion approach can be further extended by including different continuity directions for lithologies and fluids, and vertical trends in the LF proportions. Simulation-based estimation of model parameters is also possible as a result of efficiencies in the simulation algorithm.

The inversion approach is evaluated on a 2D cross section of a real reservoir in Part II of this paper.

ACKNOWLEDGMENTS

Our work was funded by the Uncertainty in Reservoir Evaluation (URE) initiative at the Norwegian University of Science and Technology (NTNU).

APPENDIX A

MARKOV RANDOM FIELD

The profile Markov random field is defined by

$$p(\boldsymbol{\pi}_{\mathbf{x}}|\boldsymbol{\pi}_{-\mathbf{x}}) = p(\boldsymbol{\pi}_{\mathbf{x}}|\boldsymbol{\pi}_{\mathbf{y}};\mathbf{y} \in \delta(\mathbf{x}));\ \text{all}\ \mathbf{x} \in \mathcal{L}_{\mathcal{D}}^{\mathbf{x}}, \tag{A-1}$$

where the profiles follow nonhomogeneous Markov-chain models given by

$$p(\boldsymbol{\pi}_{\mathbf{x}}|\boldsymbol{\pi}_{\mathbf{y}};\mathbf{y} \in \delta(\mathbf{x})) = \prod_{t} p(\pi_{\mathbf{x},t}|\pi_{\mathbf{x},t+1},\pi_{\mathbf{y},t};\mathbf{y} \in \delta(\mathbf{x}));\ \text{all}\ \mathbf{x} \in \mathcal{L}_{\mathcal{D}}^{\mathbf{x}}. \tag{A-2}$$

Using this prior model formulation, we want to show

$$p(\pi_{\mathbf{x},t}|\boldsymbol{\pi}_{-(\mathbf{x},t)}) = p(\pi_{\mathbf{x},t}|\pi_{\mathbf{x},t+1},\pi_{\mathbf{x},t-1},\pi_{\mathbf{y},t};\mathbf{y} \in \delta(\mathbf{x}));\ \text{all}\ (\mathbf{x},t) \in \mathcal{L}_{\mathcal{D}}. \tag{A-3}$$

Proof:

$$
\begin{aligned}
&p(\pi_{\mathbf{x},t}|\boldsymbol{\pi}_{-(\mathbf{x},t)}) \\
&= p(\pi_{\mathbf{x},t}|\boldsymbol{\pi}_{\mathbf{x},-t},\boldsymbol{\pi}_{\mathbf{y}};\mathbf{y}\in\delta(\mathbf{x})) = \frac{p(\pi_{\mathbf{x},t},\boldsymbol{\pi}_{\mathbf{x},-t}|\boldsymbol{\pi}_{\mathbf{y}})}{\sum_{\pi_{\mathbf{x},t}} p(\pi_{\mathbf{x},t},\boldsymbol{\pi}_{\mathbf{x},-t}|\boldsymbol{\pi}_{\mathbf{y}})} = \frac{p(\boldsymbol{\pi}_{\mathbf{x}}|\boldsymbol{\pi}_{\mathbf{y}})}{\sum_{\pi_{\mathbf{x},t}} p(\boldsymbol{\pi}_{\mathbf{x}}|\boldsymbol{\pi}_{\mathbf{y}})} \\
&= \frac{p(\pi_{\mathbf{x},T}|\pi_{\mathbf{y},T})\times\cdots\times p(\pi_{\mathbf{x},t}|\pi_{\mathbf{x},t+1},\pi_{\mathbf{y},t})\times\cdots\times p(\pi_{\mathbf{x},1}|\pi_{\mathbf{x},2},\pi_{\mathbf{y},1})}{\sum_{\pi_{\mathbf{x},t}} p(\pi_{\mathbf{x},T}|\pi_{\mathbf{y},T})\times\cdots\times p(\pi_{\mathbf{x},t}|\pi_{\mathbf{x},t+1},\pi_{\mathbf{y},t})\times\cdots\times p(\pi_{\mathbf{x},1}|\pi_{\mathbf{x},2},\pi_{\mathbf{y},1})} \\
&= \frac{p(\pi_{\mathbf{x},t+1}|\pi_{\mathbf{y},t+1})}{p(\pi_{\mathbf{x},t+1}|\pi_{\mathbf{y},t+1})}\times\frac{p(\pi_{\mathbf{x},t}|\pi_{\mathbf{x},t+1},\pi_{\mathbf{y},t})p(\pi_{\mathbf{x},t-1}|\pi_{\mathbf{x},t},\pi_{\mathbf{y},t-1})}{\sum_{\pi_{\mathbf{x},t}} p(\pi_{\mathbf{x},t}|\pi_{\mathbf{x},t+1},\pi_{\mathbf{y},t})p(\pi_{\mathbf{x},t-1}|\pi_{\mathbf{x},t},\pi_{\mathbf{y},t-1})} \\
&= \frac{p(\pi_{\mathbf{x},t+1},\pi_{\mathbf{x},t},\pi_{\mathbf{x},t-1}|\pi_{\mathbf{y},t+1},\pi_{\mathbf{y},t},\pi_{\mathbf{y},t-1})}{\sum_{\pi_{\mathbf{x},t}} p(\pi_{\mathbf{x},t+1},\pi_{\mathbf{x},t},\pi_{\mathbf{x},t-1}|\pi_{\mathbf{y},t+1},\pi_{\mathbf{y},t},\pi_{\mathbf{y},t-1})} \\
&= p(\pi_{\mathbf{x},t}|\pi_{\mathbf{x},t+1},\pi_{\mathbf{x},t-1},\pi_{\mathbf{y},t+1},\pi_{\mathbf{y},t},\pi_{\mathbf{y},t-1}) \\
&= p(\pi_{\mathbf{x},t}|\pi_{\mathbf{x},t+1},\pi_{\mathbf{x},t-1},\pi_{\mathbf{y},t};\mathbf{y}\in\delta(\mathbf{x})).
\end{aligned}
\tag{A-4}
$$

APPENDIX B

SIMULATION ALGORITHM

Initiate

Generate arbitrary $\boldsymbol{\pi}^0$

Iterate $i = 1,2,3,\ldots$

Initiate

$\boldsymbol{\pi}^i = \boldsymbol{\pi}^{i-1}$

Do

$\mathbf{x}$ in random sequence through $\mathcal{L}_{\mathcal{D}}^{\mathbf{x}}$

Upward recursion

Initiate

$$
p_u(\pi_{\mathbf{x},T}) = \begin{cases} \text{const}\times l(\mathbf{d}_{\mathbf{x}}^s|\pi_{\mathbf{x},T})p(\pi_{\mathbf{x},T}|\pi_{\mathbf{y},T}^i); & \mathbf{x}\in -\mathcal{K} \\ \text{const}\times p(d_{\mathbf{x},T}^w|\pi_{\mathbf{x},T})l(\mathbf{d}_{\mathbf{x}}^s|\pi_{\mathbf{x},T})p(\pi_{\mathbf{x},T}|\pi_{\mathbf{y},T}^i); & \mathbf{x}\in\mathcal{K} \end{cases}
$$

$$
\text{const} = [\Sigma_{\pi_{\mathbf{x},T}} p_u(\pi_{\mathbf{x},T})]^{-1}
$$

Iterate $t = T-1, T-2,\cdots,1$

$$
p_u(\pi_{\mathbf{x},t+1},\pi_{\mathbf{x},t}) = \begin{cases} \text{const}\times l(\mathbf{d}_{\mathbf{x}}^s|\pi_{\mathbf{x},t})p(\pi_{\mathbf{x},t}|\pi_{\mathbf{x},t+1},\pi_{\mathbf{y},t}^i)p_u(\pi_{\mathbf{x},t+1}); & \mathbf{x}\in -\mathcal{K} \\ \text{const}\times p(d_{\mathbf{x},t}^w|\pi_{\mathbf{x},t})l(\mathbf{d}_{\mathbf{x}}^s|\pi_{\mathbf{x},t})p(\pi_{\mathbf{x},t}|\pi_{\mathbf{x},t+1},\pi_{\mathbf{y},t}^i)p_u(\pi_{\mathbf{x},t+1}); & \mathbf{x}\in\mathcal{K} \end{cases}
$$

$$
\text{const} = [\Sigma_{\pi_{\mathbf{x},t+1}}\Sigma_{\pi_{\mathbf{x},t}} p_u(\pi_{\mathbf{x},t+1},\pi_{\mathbf{x},t})]^{-1}
$$

$$
p_u(\pi_{\mathbf{x},t}) = \Sigma_{\pi_{\mathbf{x},t+1}} p_u(\pi_{\mathbf{x},t+1},\pi_{\mathbf{x},t})
$$

End iterate t

Downward simulation

Initiate

Generate realization $\pi_{\mathbf{x},1}^c$ from $p_u(\pi_{\mathbf{x},1})$

Iterate $t = 2\ldots,T$

Generate realization $\pi_{\mathbf{x},t}^c$ from

$$
p_u(\pi_{\mathbf{x},t}|\pi_{\mathbf{x},t-1}^c) = p_u(\pi_{\mathbf{x},t},\pi_{\mathbf{x},t-1}^c)/p_u(\pi_{\mathbf{x},t-1}^c)
$$

End iterate t

Update

$\boldsymbol{\pi}_{\mathbf{x}}^i = \boldsymbol{\pi}_{\mathbf{x}}^c$

End iterate $\mathbf{x}$

End iterate i

In each iteration i, $\boldsymbol{\pi}^i$ is generated from $\tilde{p}^i(\boldsymbol{\pi}|\mathbf{d})$ with limiting distribution

$$
\lim_{i\to\infty} \tilde{p}^i(\boldsymbol{\pi}|\mathbf{d}) = \tilde{p}(\boldsymbol{\pi}|\mathbf{d}), \tag{B-1}
$$

which is the distribution of interest. One sweep of the algorithm includes $N_{\mathbf{x}}[L + (T-1)L^2]$ operations, with L being the number of LF classes and with T and $N_{\mathbf{x}}$ being the number of vertical and horizontal grid nodes. Hence, it is quadratic in the size of sample space of $\pi_{\mathbf{x},t}$ and linear in the number of grid nodes in $\mathcal{L}_{\mathcal{D}}$.

APPENDIX C

TRANSITION MATRICES IN EMPIRICAL STUDY

Transition matrices with limiting distributions in 2D Markov random-field model in the synthetic empirical study:

$$
\mathbf{P}_{SG,SG}^t = \begin{pmatrix} 0.9998 & 0 & 0 & 0.0002 \\ 0.9996 & 0.0002 & 0 & 0.0002 \\ 0.9994 & 0.0002 & 0.0002 & 0.0002 \\ 0.9994 & 0.0002 & 0.0002 & 0.0002 \end{pmatrix}
$$

$$
\mathbf{p}_{SG,SG} = (0.9997 \quad 0.0000 \quad 0.0000 \quad 0.0003)
$$

$$
\mathbf{P}_{SG,SO}^t = \begin{pmatrix} 0.9995 & 0 & 0 & 0.0005 \\ 0.4999 & 0.4999 & 0 & 0.0002 \\ 0.4998 & 0.4998 & 0.0002 & 0.0002 \\ 0.4998 & 0.4998 & 0.0002 & 0.0002 \end{pmatrix}
$$

$$
\mathbf{p}_{SG,SO} = (0.9990 \quad 0.0005 \quad 0.0000 \quad 0.0005)
$$

$$
\mathbf{P}_{SG,SB}^t = \begin{pmatrix} 0.9995 & 0 & 0 & 0.0005 \\ 0.9990 & 0.0005 & 0 & 0.0005 \\ 0.4998 & 0.0002 & 0.4998 & 0.0002 \\ 0.4998 & 0.0002 & 0.4998 & 0.0002 \end{pmatrix}
$$

$$
\mathbf{p}_{SG,SB} = (0.9990 \quad 0.0000 \quad 0.0005 \quad 0.0005)
$$

$$
\mathbf{P}_{SG,SH}^t = \begin{pmatrix} 0.5000 & 0 & 0 & 0.5000 \\ 0.4999 & 0.0002 & 0 & 0.4999 \\ 0.4998 & 0.0002 & 0.0002 & 0.4998 \\ 0.4998 & 0.0002 & 0.0002 & 0.4998 \end{pmatrix}
$$

$$
\mathbf{p}_{SG,SH} = (0.4999 \quad 0.0001 \quad 0.0001 \quad 0.4999)
$$

$$
\mathbf{P}_{SO,SO}^t = \begin{pmatrix} 0.5000 & 0 & 0 & 0.5000 \\ 0.0002 & 0.9996 & 0 & 0.0002 \\ 0.0002 & 0.9994 & 0.0002 & 0.0002 \\ 0.0002 & 0.9994 & 0.0002 & 0.0002 \end{pmatrix}
$$

$$\mathbf{p}_{SO,SO} = (0.0005 \quad 0.9990 \quad 0.0000 \quad 0.0005)$$

$$\mathbf{P}^t_{SO,SB} = \begin{pmatrix} 0.5000 & 0 & 0 & 0.5000 \\ 0.0005 & 0.9990 & 0 & 0.0005 \\ 0.0002 & 0.4998 & 0.4998 & 0.0002 \\ 0.0002 & 0.4998 & 0.4998 & 0.0002 \end{pmatrix}$$

$$\mathbf{p}_{SO,SB} = (0.0010 \quad 0.9970 \quad 0.0010 \quad 0.0010)$$

$$\mathbf{P}^t_{SO,SH} = \begin{pmatrix} 0.0005 & 0 & 0 & 0.9995 \\ 0.0002 & 0.4999 & 0 & 0.4999 \\ 0.0002 & 0.4998 & 0.0002 & 0.4998 \\ 0.0002 & 0.4998 & 0.0002 & 0.4998 \end{pmatrix}$$

$$\mathbf{p}_{SO,SH} = (0.0002 \quad 0.4997 \quad 0.0001 \quad 0.4999)$$

$$\mathbf{P}^t_{SB,SB} = \begin{pmatrix} 0.5000 & 0 & 0 & 0.5000 \\ 0.3333 & 0.3333 & 0 & 0.3333 \\ 0.0002 & 0.0002 & 0.9994 & 0.0002 \\ 0.0002 & 0.0002 & 0.9994 & 0.0002 \end{pmatrix}$$

$$\mathbf{p}_{SB,SB} = (0.0007 \quad 0.0004 \quad 0.9981 \quad 0.0007)$$

$$\mathbf{P}^t_{SB,SH} = \begin{pmatrix} 0.0005 & 0 & 0 & 0.9995 \\ 0.0005 & 0.0005 & 0 & 0.9990 \\ 0.0002 & 0.0002 & 0.4998 & 0.4998 \\ 0.0002 & 0.0002 & 0.4998 & 0.4998 \end{pmatrix}$$

$$\mathbf{p}_{SB,SH} = (0.0002 \quad 0.0002 \quad 0.4995 \quad 0.5000)$$

$$\mathbf{P}^t_{SH,SH} = \begin{pmatrix} 0.0002 & 0 & 0 & 0.9998 \\ 0.0002 & 0.0002 & 0 & 0.9996 \\ 0.0002 & 0.0002 & 0.0002 & 0.9994 \\ 0.0002 & 0.0002 & 0.0002 & 0.9994 \end{pmatrix}$$

$$\mathbf{p}_{SH,SH} = (0.0002 \quad 0.0002 \quad 0.0002 \quad 0.9993)$$

with the term $\mathbf{P}^t_{(\cdot,\cdot)}$ corresponding to the transition matrix with lateral neighbors $(\cdot,\cdot)$ and $\mathbf{p}_{(\cdot,\cdot)}$ the corresponding limiting distribution.

The average of the transition matrices is

$$\mathbf{P} = \begin{pmatrix} 0.5000 & 0 & 0 & 0.5000 \\ 0.3333 & 0.3333 & 0 & 0.3333 \\ 0.2500 & 0.2500 & 0.2500 & 0.2500 \\ 0.2500 & 0.2500 & 0.2500 & 0.2500 \end{pmatrix}$$

with associated limiting distribution

$$\mathbf{p} = (0.3529 \quad 0.1765 \quad 0.1176 \quad 0.3529).$$

Transition matrix in profilewise Markov-chain model is

$$\mathbf{P} = \begin{pmatrix} 0.9001 & 0 & 0 & 0.0999 \\ 0.0531 & 0.8913 & 0 & 0.0557 \\ 0.0030 & 0.0560 & 0.9065 & 0.0345 \\ 0.0129 & 0.0097 & 0.0787 & 0.8987 \end{pmatrix}$$

with limiting distribution

$$\mathbf{p} = (0.1544 \quad 0.1870 \quad 0.3010 \quad 0.3576).$$

REFERENCES

Aki, K., and P. G. Richards, 1980, Quantitative seismology: Theory and methods: W.H. Freeman & Co.

Avseth, P., T. Mukerji, and G. Mavko, 2005, Quantitative seismic interpretation: Applying rock physics tools to reduce interpretation risk: Cambridge University Press.

Bosch, M., C. Carvajal, J. Rodrigues, A. Torres, M. Aldana, and J. Sierra, 2009, Petrophysical seismic inversion conditioned to well-log data: Methods and application to a gas reservoir: Geophysics, **74**, no. 2, O01–O15.

Buland, A., O. Kolbjørnsen, R. Hauge, Ø. Skjæveland, and K. Duffaut, 2008, Bayesian lithology and fluid prediction from seismic prestack data: Geophysics, **73**, no. 3, C13–C21.

Buland, A., O. Kolbjørnsen, and H. Omre, 2003, Rapid spatially coupled AVO inversion in the Fourier domain: Geophysics, **68**, 824–836.

Buland, A., and H. Omre, 2003a, Bayesian linearized AVO inversion: Geophysics, **68**, 185–198.

——–, 2003b, Bayesian wavelet estimation from seismic and well data: Geophysics, **68**, 2000–2009.

Chib, S., 1996, Calculating posterior distributions and modal estimates in Markov mixture models: Journal of Econometrics, **75**, 79–97.

Contreras, A., C. Torres-Verdin, W. Chesters, K. Kvien, and M. Globe, 2005, Joint stochastic inversion of petrophysical logs and 3D pre-stack data to assess the spatial continuity of fluid units away from wells: Application to a Gulf-of-Mexico deepwater hydrocarbon reservoir: 46th Annual Logging Symposium, Society of Professional Well Log Analysts, Paper UUU.

Eidsvik, J., P. Avseth, H. Omre, T. Mukerji, and G. Mavko, 2004, Stochastic reservoir characterization using prestack seismic data: Geophysics, **69**, 978–993.

González, E. F., T. Mukerji, and G. Mavko, 2008, Seismic inversion combining rock physics and multiple-point geostatistics: Geophysics, **73**, no. 1, R11–R21.

Larsen, A. L., M. Ulvmoen, H. Omre, and A. Buland, 2006, Bayesian lithology/fluid prediction and simulation on the basis of a Markov-chain prior model: Geophysics, **71**, no. 5, R69–R78.

Mallick, S., 2007, Amplitude-variation-with-offset, elastic-impedence, and wave-equation synthetics — A modeling study: Geophysics, **72**, no. 1, C1–C7.

Ulvmoen, M., and H. Hammer, 2010, Bayesian lithology/fluid inversion — comparison of two algorithms: Computational Geosciences, **14**, 357–367.

Ulvmoen, M., H. Omre, and A. Buland, 2010, Improved resolution in Bayesian lithology/fluid inversion from prestack seismic data and well observations: Part 2 — Real case study: Geophysics, this issue.

Winkler, G., 1995, Image analysis, random fields and Markov chain Monte Carlo methods: Springer.